O'KEEFE, M. A. (1979). 37th Annu. Proc. EMSA, Vol. 1, pp. 556-557. Baton Rouge: Claitor.

PERRIN, R. C., ENGLERT, A. & BULLOUGH, R. (1972). Interatomic Potentials and Simulation of Defects, edited by P. C. GEHEN, J. R. BELLER JR & R. I. JAFFEE, p. 509, New York: Plenum.

SINCLAIR, R., PONCE, F. A., YAMASHITA, T., SMITH, D. J., CAMPS, R. A., FREEMAN, L. A., ERASMUS, S. J., NIXSON, W. C., SMITH, K. C. A. & CATTO, C. J. D. (1982). Nature (London), 298, 127-131.

TAKAI, Y., HASHIMOTO, H. & ENDOH, H. (1983). Acta Cryst. A39, 516-522.

TAKAI, Y., HASHIMOTO, H., ENDOH, H. & AJIKA, N. (1981). Proc. 61st EMAG Conf., Cambridge, England, pp. 361-364.

TUNSTALL, W. J., HIRSCH, P. B. & STEEDS, J. (1964). Philos. Mag. 9, 99-119.

WHELAN, M. J., HIRSCH, P. B., HORN, R. W. & BOLLMANN, W. (1957). Proc. R. Soc. London Ser. A, 240, 524-538.

Long-Period Structures in the Nb–Ga System

BY M. TAKEDA,* G. VAN TENDELOO AND S. AMELINCKX

University of Antwerp, RUCA, Groenenborgerlaan 171, B-2020 Antwerp, Belgium

Abstract

The alloys $NbGa_{3-x}$ form composition-driven long-period superstructures derived from the DO_{22} by the introduction of non-conservative antiphase boundaries along (001) planes. The displacement vectors of successive antiphase boundaries are alternately $\frac{1}{4}$ [201] and $\frac{1}{4}$ [021]. In alloys with a composition which deviates less from $NbGa_3$ than Nb_5Ga_{13} successive antiphase boundaries all have the same displacement vector, either $\frac{1}{4}$ [201] or $\frac{1}{4}$ [021]. The alloy Nb_5Ga_{13} is the first material which has a long-period superstructure based on the alternation of two types of antiphase boundaries.

1. Introduction

In a recent paper (Takeda, Van Tendeloo & Amelinckx, 1987) we reported briefly on a redetermination of the structure of Nb_5Ga_{13}. It was found that this structure is tetragonal and has an unusually large c parameter of ~80 Å. The structure is a long-period antiphase-boundary modulated superstructure of the DO_{22} structure. The superstructure is composition driven; the excess niobium as compared to the ideal composition $NbGa_3$ of the DO_{22} structure is accommodated in this structure along non-conservative antiphase boundaries, belonging alternately to two different families. In the present paper we report more detailed results on Nb_5Ga_{13} as well as on the structures of alloys in the same binary system but with a slightly different composition.

---

* On leave from Toyohashi University of Technology, 1-1 Hibarigaoka, Tenpakucho, Toyohashi 440, Japan.

2. Preparation of materials and specimens

The alloys were prepared by alloying the elements in the appropriate proportions by dissolving niobium in molten gallium. The molten mixture was then quenched to room temperature and subsequently annealed at 1370 K, which is below the peritectic decomposition temperature of 1508 K, over 14 d. Specimens for electron microscopy and electron diffraction are prepared by crushing the brittle material. We prepared and examined alloys with a nominal composition in the range between Nb_4Ga_{10} and $NbGa_3$.

3. Crystallographic considerations; structural building principle

The structure of Nb_5Ga_{13} was determined by Schubert (1964). It was found to be a long-period out-of-phase boundary modulated superstructure derived from the deformed DO_{22} structure of $NbGa_3$, which is itself a superstructure derived from a face-centred-based $L1_2$ structure. The DO_2 structure is derived from the $L1_2$ structure by the introduction of periodic *conservative* antiphase boundaries. On the other hand the Nb_5Ga_{13} structure is derived from the DO_{22} structure by the introduction of *non-conservative* out-of-phase boundaries after every two DO_{22} unit cells. In the model of Schubert (Fig. 1b) all the out-of-phase boundaries have the same displacement vector; we shall show that the essential features of the model are correct, but that the out-of-phase boundaries have alternately two different displacement vectors, which are related by the tetragonal symmetry of the DO_{22} basic structure (Figs. 1a,c). As a result the long period

along the tetragonal axis is doubled compared with that of the Schubert structure (Takeda, Van Tendeloo & Amelinckx, 1987). The crystallographic data regarding the two structures are compared in Table 1.

To our surprise we found that if the composition is such that the domain size is larger than $2c_{D0_{22}}$ the building principle of Schubert is found to be realized, i.e. in any given orientation variant all out-of-phase boundaries have the same displacement vector. Two coaxial variants, each built on a single family of out-of-phase boundaries, are found to occur in separate regions of the specimen.

The two families of out-of-phase boundaries have displacement vectors of the type $\frac{1}{4}$ $[201]_{D0_{22}}$ and $\frac{1}{4}$ $[021]_{D0_{22}}$; note that the sum of these two vectors is a lattice vector $\frac{1}{2}$ [111] of the $D0_{22}$ structure. We will show that whereas these two displacement vectors occur alternately at successive out-of-phase boundaries within the unit cell of Nb_5Ga_{13}, they occur in separate domains in the alloys containing domain strips wider than $2c_{D0_{22}}$.

Both types of out-of-phase boundaries are equivalent in accommodating an excess of niobium. The number n of f.c.c. unit cells in the long period can immediately be deduced from the number of interspot spacings between 000 and $(004)_{D0_{22}}$. Since in the long-period unit cell there are two domain

Table 1. *Lattice parameters and space groups of different phases* Nb_xGa_y

	Nb_xGa_y					c/a ratio	Space
n	x	y	a	b	c	of $D0_{22}$	group
9	5	13	0·378	0·378	8·02	2·35	$I4_1/amd$
11	6	16	0·378	0·378	2·44	2·35	$Bmm2$
13	7	19	0·378	0·378	2·87	2·34	$Bmmm$
15	8	22	0·378	0·378	3·32	2·34	$Bmm2$

strips and two out-of-phase boundaries each with a 'thickness' of one half a f.c.c. unit cell, one finds for the number of f.c.c. unit cells in one domain strip $(n-1)/2$. The number of (001) atom layers in one domain is then again $2[(n-1)/2]+1 = n$; among these there are $(n+1)/2$ layers with composition NbGa and $(n-1)/2$ layers with composition 2Ga. The ideal macroscopic composition is thus $Nb_{(n+1)/2}Ga_{(3n-1)/2}$. The number of $D0_{22}$ unit cells in one domain strip is evidently $(n-1)/4$. If we assume that under the imaging conditions used only the columns of minority atoms produce bright dots, the number of rows of bright dots in one domain strip is equal to $(n+1)/2$; these simple relationships allow one to deduce the ideal composition directly from a high-resolution image.

4. Electron diffraction patterns

4.1. *The alloy* Nb_5Ga_{13}

Fig. 2 shows the electron diffraction patterns respectively along [001], [1$\bar{1}$0] and [100] obtained from a specimen with nominal composition Nb_5Ga_{13} ($n = 9$). The pattern along the [001] zone (Fig. 2a) exhibits clearly the tetragonal symmetry of the lattice. The [100] zone diffraction pattern (Fig. 2c) reveals a long period, as deduced from the spot separation, equal to 18 times the period associated with one f.c.c. cube. The crosses indicate the positions of the $D0_{22}$ diffraction spots. Furthermore it is noted that the 01l of superlattice spots is shifted over half of the interspot spacing with respect to the spots in the 00l row (Fig. 3); characters in large letters indicate indices with respect to the $D0_{22}$ lattice; those in small characters are indices referring to the superlattice. This
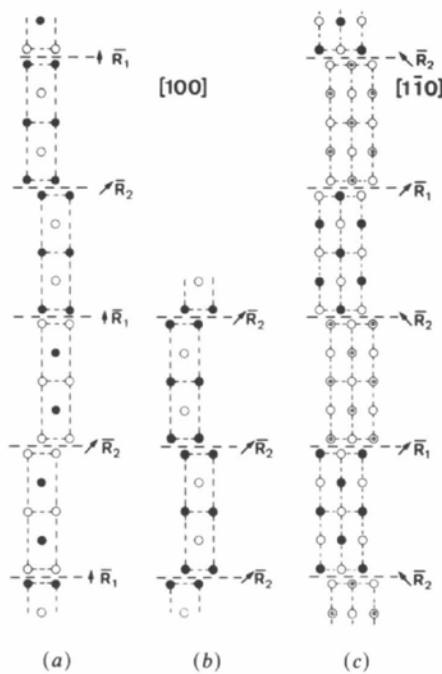

Fig. 1. The structure of Nb_5Ga_{13}. (a) Model deduced from the present study; two types of antiphase boundaries alternate; view along the [100] zone. (b) Model according to Schubert, all antiphase boundaries are of the same type; view along the [010] zone. (c) Model of the structure projected along the [110] zone; all antiphase boundaries have similar projections for both models.
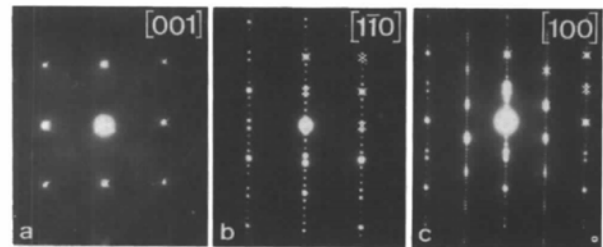

Fig. 2. Electron diffraction patterns of the Nb_5Ga_{13} structure. (a) [001] zone, (b) [1$\bar{1}$0] zone, (c) [100] zone. The crosses mark the positions of $D0_{22}$ diffraction spots.

shows that the reciprocal lattice is centred as represented in Fig. 4; the $(004)_{D0_{22}}$ reflection should thus be given the indices 0,0,36 in the superlattice. The superlattice indices are indicated in parentheses in Fig. 4. The c parameter is therefore equal to ~36 times the size of the basic f.c.c. unit cell. The $[1\bar{1}0]$ zone pattern of Fig. 2(b) confirms the reciprocal lattice of Fig. 4.

The intensity distribution clearly shows pronounced maxima around the positions marked by crosses in Fig. 4; these are positions of the reciprocal lattice of the basic $D0_{22}$ structure. This is a strong indication that the long-period structure is a modulated derivative of the $D0_{22}$ structure. The indices with respect to the $D0_{22}$ lattice are indicated in Fig. 4 without brackets.

There are no 'fractional' shifts of the sequences of superstructure spots with respect to the positions of the $D0_{22}$ spots indicated by crosses. If we assume the structure to be modulated by interfaces which all have the same displacement vector this would mean that the displacement vector of out-of-phase boundaries should be a lattice vector. This is of course an internal contradiction. The next simplest assumption is that

within the repeat period at least two types of different interfaces, for which the sum of the displacement vectors is a lattice vector, alternate. These two vectors should moreover be such that the resulting structure is consistent with the tetragonal symmetry. Further, below, we deduce the displacement vector of these interfaces in a systematic manner. Note that the weak spots along the $00l$ row are due to double diffraction out of the $01l$ rows.

4.2. The alloys Nb_6Ga_{16} and Nb_7Ga_{19}

The diffraction patterns of these two alloys are very similar; they only differ in the spacing of the superstructure spots. Although the [001] zone pattern is still consistent with a tetragonal lattice, the [100] and [010] zones are no longer identical; the symmetry of the structures must thus be lower, *i.e.* orthorhombic, pseudo-tetragonal. The intensity maxima still occur in the vicinity of the $D0_{22}$ spot positions, which means that the superstructure is still a long-period variant of the $D0_{22}$ basic structure.

The long period now corresponds with ~13 times (or 11 times) the size of the f.c.c. cell. The centring along the [010] zone causes the lattice parameter to
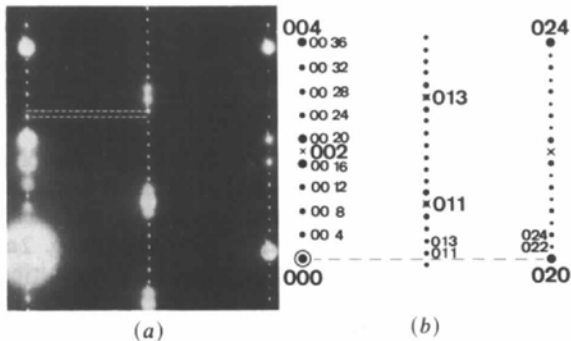

Fig. 3. (a) Magnified view of the electron diffraction pattern along the [100] zone. Note that the $00l$ and $01l$ sequences of diffraction spots are shifted one relative to the other by half of an interspot spacing, as shown schematically in (b).
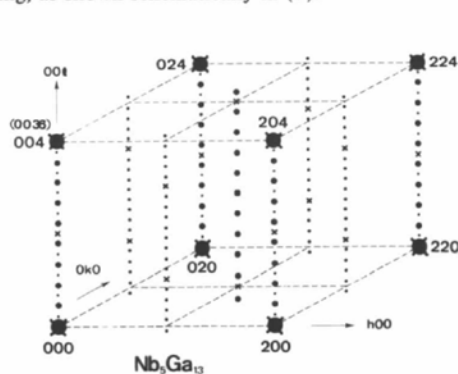

Fig. 4. Reciprocal lattice of the tetragonal Nb_5Ga_{13} structure observed in this work. The small full dots represent double diffraction spots; the crosses represent the positions of the reciprocal lattice of the tetragonal $D0_{22}$ structure. The corresponding lattice is body centred.
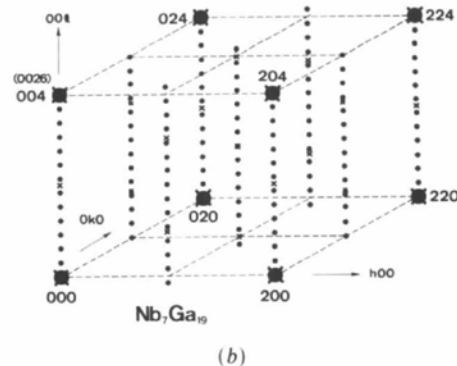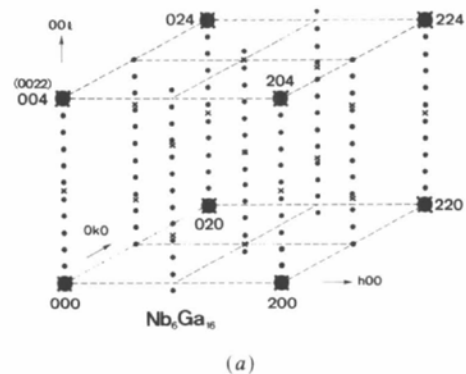

Fig. 5. Reciprocal lattice of the orthorhombic (a) Nb_6Ga_{16} and (b) Nb_7Ga_{19} structures. The two reciprocal lattices differ only in the long period, *i.e.* in the separation of the superstructure spots. The lattice is B-face centred. The positions of the $D0_{22}$ spots are indicated by crosses.

be doubled, *i.e.* equal to 26 (or 22) times the size of the basic cubic cell. The absence of centring along the [100] zone (Fig. 6a) shows that the lattice is thus orthorhombic *B*-face centred. The reciprocal lattices are represented in Figs. 5(a), (b). The [110] zone pattern of Fig. 6 of the compound Nb_7Ga_{19} is consistent with the reciprocal lattices of Fig. 5.

In order to be present the indices have to satisfy the following conditions: for $00l$, $l = 2n$; for $h0l$, $h + l = 2n$; for $h00$, $h = 2n$; and for $hk0$, $h = 2n$; for hkl, $h + l = 2n$. These reflections are consistent with a number of space groups; in particular with $Bmm2$ and $Bmmm$.

It is noted that in the two alloys the sequences of superstructure spots are fractionally shifted with respect to the $D0_{22}$ spot positions. The observed fractional shifts are indicated in Table 2; they are the same for both alloys.

From the [001] zone pattern we deduce that the lattice is tetragonal within experimental error although the structures are orthorhombic; from the

(a)

(b)

Fig. 6. Diffraction patterns of (a) the Nb_6Ga_{16} structure along the [100] zone and (b) the Nb_7Ga_{19} structure along the [1$\bar{1}$0] zone. These patterns can be compared with the corresponding sections of the reciprocal lattice of Fig. 5.

[100] and [010] zones we deduce that the c/a ratio of the basic $D0_{22}$ lattice differs significantly from 2; it is $c/a = 2 \cdot 34$, *i.e.* the $D0_{22}$ unit cell is elongated along the c [001] direction.

The lattice parameters of the different phases observed here are summarized in Table 1.

5. Structural models

5.1. Nb_5Ga_{13} $(n = 9)$

In previous papers we have made extensive use of the method of 'fractional shifts' to determine structural models of long-period antiphase boundary structures, based exclusively on geometrical features of the diffraction pattern. This method leads to an unambiguous result in cases where the basic structure is known and where the antiphase boundaries in any parallel set all have the same displacement vector. In cases where the parallel antiphase boundaries have alternately two different displacement vectors R_1 and R_2, the method makes it possible to determine the sum $R_1 + R_2$ only (Van Tendeloo, Wolf, Van Landuyt & Amelinckx, 1978). The high-resolution images will show that this is the situation in the present case; we shall show that nevertheless the analysis of the diffraction pattern allows us to derive a model by systematic deduction.
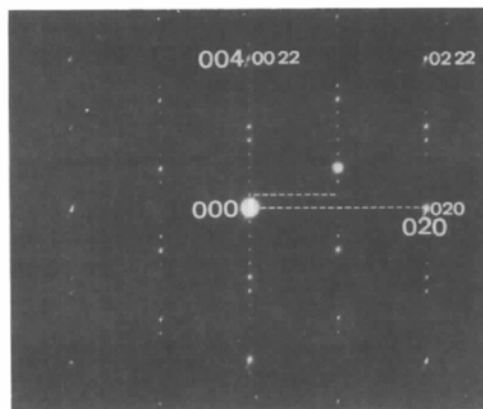
From the reinforcements of the spot intensities we deduce that the basic structure is the $D0_{22}$ phase. From the spot separation in the [100] zone pattern we find that the long spacing is 40 Å or a multiple of this. The sequences of superstructure spots do not exhibit fractional shifts with respect to the basic $D0_{22}$ spots; this leads to the conclusion that $g \cdot R = 0$ for all g; *i.e.* R must be a lattice vector of the $D0_{22}$ structure, which would mean that R cannot be the displacement vector of an antiphase boundary; the next simplest assumption is then that $R = R_1 + R_2$, where R_1 and R_2 occur alternately.

Although the sequences of superstructure spots are not fractionally shifted, one row is shifted relative to the next row over half of the interspot spacing. This must be attributed to centring of the projected unit mesh along this zone. The long spacing is thus in fact 80 Å.
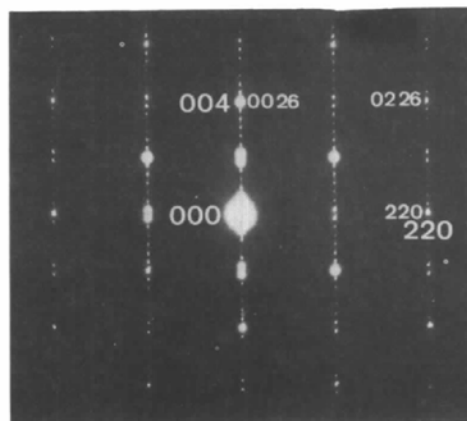
Along the [110] zone the spot separation is doubled compared with that along the [100] zone, from which we conclude that the separation of interfaces, which are now equivalent in projection along [110], is 20 Å. The projections of the two displacement vectors R_1 and R_2 along the [110] zone should then also be equivalent. This common projected displacement vector can be deduced from the observed fractional shifts along the [110] zone.

The fractional shifts are $\frac{1}{2}$ or 0 (mod 1). Let us call $R = [uvw]$; we then have from the fractional shifts

$$h(u + v) + lw = 0 \pmod{1} \qquad (1)$$

if

$$2h + l = 4p; \tag{2}$$

$$h(u + v) + lw = \tfrac{1}{2} \ (\text{mod } 1) \tag{3}$$

if

$$2h + l = 4q \pm 2 \tag{4}$$

where p and q are integers.

Substituting (2) and (4) into (1) and (3) leads to the equations

$$h(u + v - 2w) = 4pw \tag{5}$$

$$h(u + v - 2w) = (4q \pm 2)w \pm \tfrac{1}{2}; \tag{6}$$

subtraction leads to

$$[4(p - q) \pm 2]w = \pm \tfrac{1}{2} \ (\text{mod } 1). \tag{7}$$

The solution corresponding to $p = q$ is $w = \pm \tfrac{1}{4}$ (mod 1). This solution also satisfies (7) for all values of p and q. With $w = \tfrac{1}{4}$ the relations (5) and (6) reduce to

$$h(u + v - \tfrac{1}{2}) = p \ (\text{mod } 1) \tag{8}$$

$$h(u + v - \tfrac{1}{2}) = q \ (\text{mod } 1) \tag{9}$$

for all h, of which the simplest solution is

$$u + v = \tfrac{1}{2} \tag{10}$$

The $\mathbf{R}_1$ and $\mathbf{R}_2$ must moreover be of the type usually met in f.c.c.-based alloys, i.e. $\tfrac{1}{2} \langle 110 \rangle$, which is equivalent to $\mathbf{R}_1 = \tfrac{1}{4} [0, \pm 2, \pm 1]$ and $\mathbf{R}_2 = \tfrac{1}{4} [\pm 2, 0, \pm 1]$ when referred to the $D0_{22}$ unit cell; the solutions of (10) are either $u = 0$, $v = \tfrac{1}{2}$ or $u = \tfrac{1}{2}$, $v = 0$. One finally notes that with $u = 0$, $v = \tfrac{1}{2}$, $w = \tfrac{1}{4}$ and $u = \tfrac{1}{2}$, $v = 0$, $w = \tfrac{1}{4}$, the following relation holds:

$$\tfrac{1}{4} [021] + \tfrac{1}{4} [201] = \tfrac{1}{2} [111],$$

which is a lattice vector of the $D0_{22}$ structure, consistent with the fact that the sum of the two displacement vectors must be a lattice vector.

5.2. Nb₆Ga₁₆, Nb₇Ga₁₉ and Nb₈Ga₂₂

The unit-cell size can immediately be determined from the superstructure spot spacing. The numbers of f.c.c. unit cells in one domain of the superstructure unit cells are respectively 11, 13 and 15, as can be deduced immediately from the number of superlattice spacings between the origin and 004. The interfaces are perpendicular to the [001] direction. The structures will be determined completely if the displacement vector of the out-of-phase boundaries is known. This vector follows directly from the fractional shifts by means of the following reasoning.

The observed fractional shifts are summarized in Table 2. If the displacement vector is represented as $R(uvw)$ the fractional shifts lead to the following

Table 2. *Observed and calculated fractional shifts in* Nb_6Ga_{16}

g	g . R (measured)	g . R (calculated)
002	$\tfrac{1}{2}$	$\tfrac{1}{2}$
004	0	1
110	$\tfrac{1}{2}$	$\tfrac{1}{2}$
101	$\pm\tfrac{1}{4}$	$\tfrac{3}{4}$
103	$\pm\tfrac{1}{4}$	$\tfrac{5}{4}$
112	0	1

independent relations:

$4w = 0 \ (\text{mod } 1)$: $\qquad w = \pm\tfrac{1}{4}$;

$u + w = \pm\tfrac{1}{4} \ (\text{mod } 1)$: $\qquad u = \pm\tfrac{1}{4} \pm \tfrac{1}{4}$,

$v + w = \pm\tfrac{1}{4} \ (\text{mod } 1)$: $\qquad v = \pm\tfrac{1}{4} \pm \tfrac{1}{4}$, i.e. $v = \pm\tfrac{1}{2}$ or 0.

The two possible displacement vectors are thus

$$\mathbf{R}_1 = \tfrac{1}{4} [201] \quad \text{and} \quad \mathbf{R}_2 = \tfrac{1}{4} [021].$$

They are consistent with all other fractional shifts, as can be deduced from Table 2.

The models for these structures are hence as represented in Figs. 7 and 8 respectively for $n = 11$ and 13. Each of these structures occurs as two coaxial variants with their c axes parallel to the same c axis of the underlying $D0_{22}$ structure.

6. High-resolution images

6.1. Nb₅Ga₁₃

The [100] zone image of this phase is reproduced in Fig. 9; it is clear that the out-of-phase boundaries
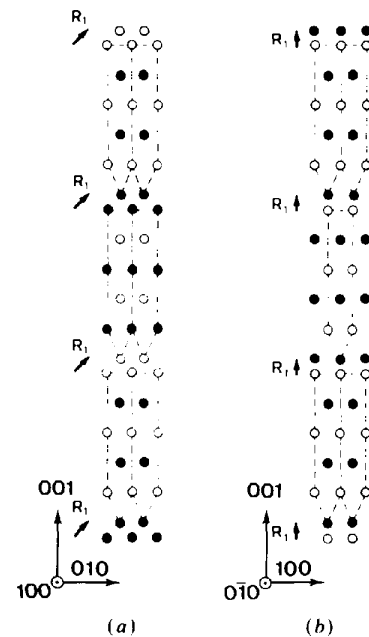

Fig. 7. Schematic representation of the structure of Nb₆Ga₁₆ ($n = 11$) as viewed along two different zones; only minority atoms are represented. (a) [100] zone, (b) [0$\bar{1}$0] zone.
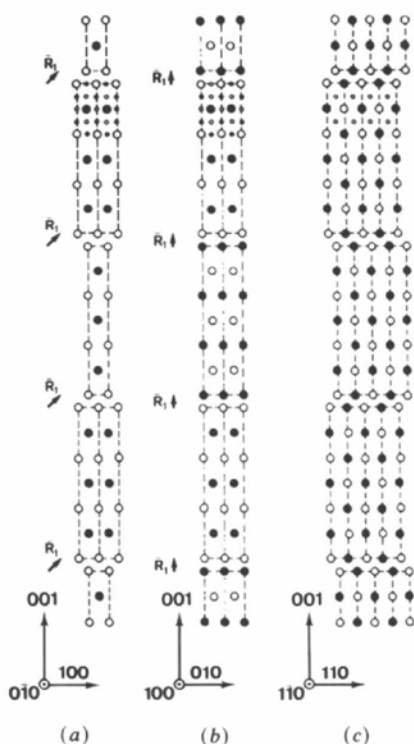
Fig. 8. Schematic representation of the structure of Nb_7Ga_{19} ($n =$ 13) structure as viewed along different zones: only minority atoms are represented. (a) [0$\bar{1}$0] zone, (b) [100] zone, (c) [1$\bar{1}$0] zone.

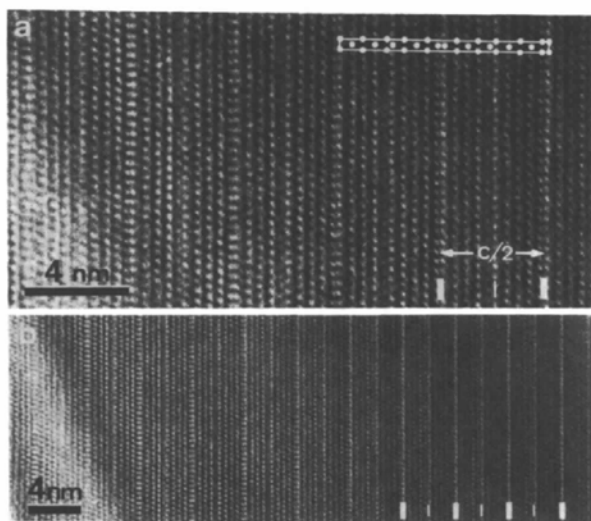are imaged as singular lines parallel to the traces of the (001) planes. Successive interfaces are imaged differently; the arrangements along the interfaces can be recognized and found to be as represented in Fig. 2(a). In the inset of Fig. 9(a) the model structure is compared with the observed image.

The domain strips are $2c_{D0_{22}}$ wide, i.e. they contain two unit cells of the $D0_{22}$ structure; the interface regions are furthermore one half of a face-centred cubic cell 'thick'; the effective width of one domain strip is thus $4+(\frac{1}{2})$ f.c.c. unit cells wide. There are four domain strips in the c repeat, i.e. the unit cell is 18 f.c.c. unit cells high.

Fig. 10 shows the high-resolution image along the [1$\bar{1}$0] zone. Along this zone the projected atom configurations are the same along all interfaces, as represented schematically in Fig. 2(c). The model structure is compared with the high-resolution image in the inset of Fig. 10. The images are obviously in agreement with the model as deduced above from the diffraction pattern.

6.2. The alloys $Nb_{(n+1)/2}Ga_{(3n-1)/2}$ ($n = 11, 13, 15$)

The [100] zone image of the alloy Nb_6Ga_{16} is reproduced in Fig. 11. All (001) interfaces are now imaged similarly, the displacement vector being inclined with respect to the interface plane. Each domain strip contains $2 \cdot 5$ $D0_{22}$ unit cells; the interfaces have a 'thickness' of one half of a f.c.c. unit cell. In the c repeat distance there are two domain strips each $5+(\frac{1}{2})$ f.c.c. unit cells wide, i.e. the c parameter has a length equal to 11 unit cells.

The [1$\bar{1}$0] zone image of the alloy with $n = 13$ is reproduced in Fig. 12; each domain strip is now $3+\frac{1}{4}$ $D0_{22}$ unit cells wide.

7. Image simulations

We have simulated images by computer for the alloy Nb_5Ga_{13} which contains the two types of out-of-phase

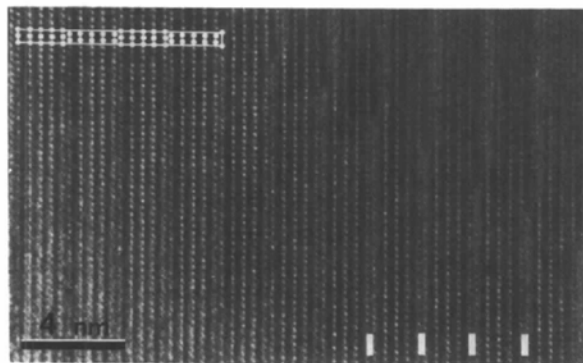Fig. 9. High-resolution image along the [100] zone of the structure of Nb_5Ga_{13}. (a) High magnification: a schematic representation of the structure is projected on the observed image. (b) Low magnification; the difference in contrast of the two families of antiphase boundaries is indicated schematically by means of bars of two different thicknesses.

Fig. 10. High-resolution images along the [1$\bar{1}$0] zone of the structure of Nb_5Ga_{13}. A schematic representation of the structure is superimposed on the observed image; all antiphase boundaries are now imaged similarly.

boundaries simultaneously. Since it is expected that the characteristics of images of out-of-phase boundaries will not be influenced in an appreciable manner by differences in their separation we have limited ourselves to this one structure.

The images were calculated for four different thicknesses and for ten different defocus values along two different zone axes, [100] and [1$\bar{1}$0] (Fig. 14). Use was made of the direct-space method developed by Van Dyck & Coene (1984). The origin, *i.e.* the left bottom corner, was chosen in a column composed of gallium and niobium atoms. The following electron-optical parameters were used for all images: spherical aberration constant $C_s = 1 \cdot 2$ mm, beam divergence $a = 0 \cdot 8$ mrad, defocus spread 7 nm. The beams up to $5 \cdot 5$ nm^{-1} were included in the aperture.
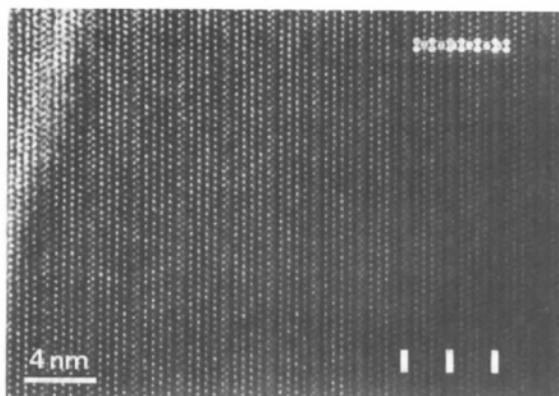

Fig. 11. High-resolution image along the [100] zone of the alloy Nb$_6$Ga$_{16}$ ($n = 11$). A schematic model at the same magnification as the photograph is superimposed on the image.

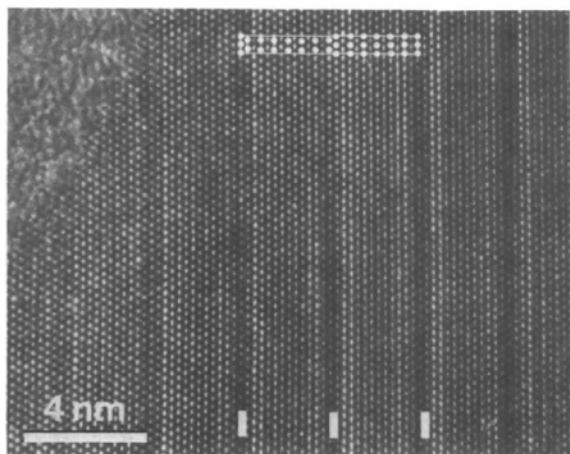Fig. 12. High-resolution images along the [1$\bar{1}$0] zone of the alloy Nb$_7$Ga$_{19}$ ($n = 13$). A schematic model at the same scale as the image is superimposed on the photograph.

7.1. *The* [100] *zone* (*Fig.* 13)

Under most contrast conditions the configurations of minority atoms can clearly be recognized in the [100] zone, either as bright dots (at $t = 5 \cdot 30$, $\Delta f = 0$ nm) or as dark dots (at $t = 5 \cdot 30$, $\Delta f = -40$ nm). The two types of antiphase boundaries I and II can further easily be distinguished from the configuration of bright dots as in the image of $t = 7 \cdot 95$ and $\Delta f = -20$ nm.

The simulated images of the out-of-phase boundaries are all either symmetrical with respect to the boundary plane (type I) or else the two parts of the image on either side of the boundary plane are related by a glide mirror operation (type II). However, this is only the case if the electron beam is assumed to be incident exactly along the zone axis. This condition was apparently realized in Fig. 11. However, in the experimental image of Fig. 9 the two rows of dots on either side of the type II out-of-phase boundaries have a different brightness. It was shown previously that such effects result from very small deviations from the exact zonal incidence (Coene, Bender, Lovey, Van Dyck & Amelinckx, 1985).

7.2. *The* [1$\bar{1}$0] *zone images*

In the experimental images of Fig. 12 the bright dots exhibit a configuration which is the same as that of the mixed-atom columns along this zone. This
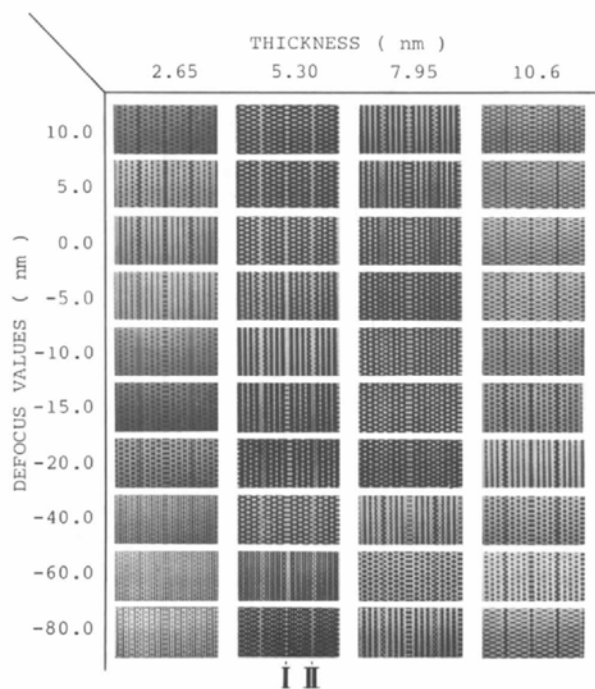

Fig. 13. Computer-simulated images along the [100] zone for four different thicknesses and ten different defocus values.

image can be compared with the model of Fig. 2(c) and with the computed images of Fig. 14: $\Delta f = -5$ to -10 nm and $t = 8 \cdot 02$ or $10 \cdot 7$ nm.

It is worth noting that the computed image at $t = 2 \cdot 67$ and $\Delta f = -10$ or -15 nm exhibits bright dots also at positions which correspond with majority atoms, i.e. all atom columns are imaged as bright dots. This is a rather common feature in ordered alloys; at sufficiently small thickness all atom columns are imaged as bright dots, whereas at larger thicknesses only minority-atom columns are imaged in this way.

In certain experimental images, such as Fig. 12, the oblique rows of bright dots hardly suffer any offset on intersecting the out-of-phase boundaries and hardly exhibit any change of spacings of the rows of dots parallel with the boundary. The out-of-phase boundaries are mainly imaged by an intensity variation, i.e. by a broad dark line.

This behaviour can be observed in Fig. 14 for $\Delta f = -15$ to 20 nm at a thickness of $8 \cdot 02$ nm; the effect of the out-of-phase boundary on the positions and on the spacing of the bright dots is very small, but the brightness is locally smaller; a dark line occurs at the boundaries, as in the experimental images.

8. Superstructure antiphase boundaries

Occassionally singular antiphase boundaries along a $(111)_{D0_{22}}$ plane occur in the long-period superstructure, intersecting the structural antiphase boundaries situated in (001) planes, as in Fig. 15. A model of
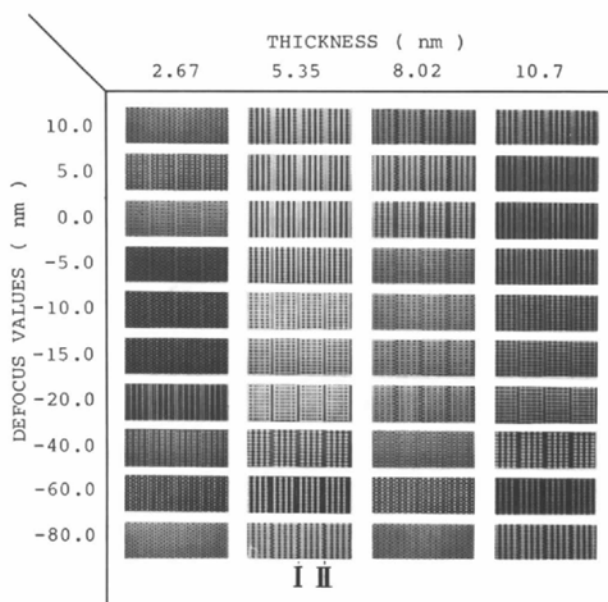
this defect as viewed along $[1\bar{1}0]$ is represented schematically in Fig. 16. The displacement vector must be such that the atom positions of the $D0_{22}$ structure are continuous across this antiphase boundary within each strip domain of the superstructure.

Two possible vectors are compatible with this observation: $\mathbf{R} = \frac{1}{2} [001]$ or $\frac{1}{2} [111]$ referred to the $D0_{22}$ structure. In the last case the singular antiphase boundary would only be revealed by the ledges in the structural antiphase boundaries. However, the perfect alignment of these ledges along a $(111)_{D0_{22}}$ plane suggests that an interface should be present also within the strip domains. It is therefore more probable that the displacement vector is $\frac{1}{2} [001]$. The model represented in Fig. 16 is based on this vector.
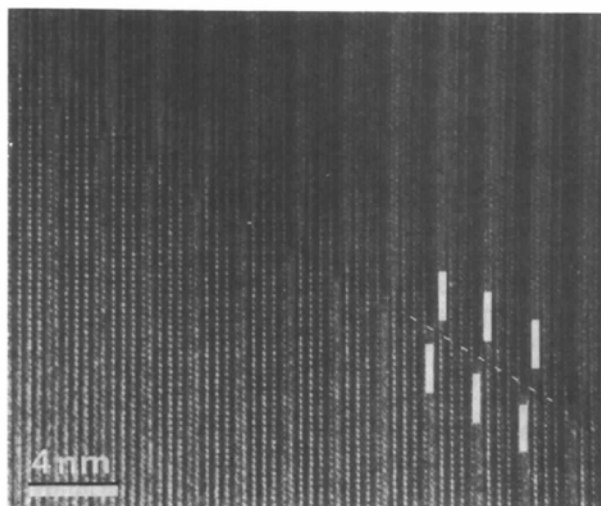

Fig. 15. Antiphase boundary in the long-period superstructure viewed along $[1\bar{1}0]_{D0_{22}}$.

Fig. 14. Computer-simulated images along the $[1\bar{1}0]$ zone for four different thicknesses and different defocus values.
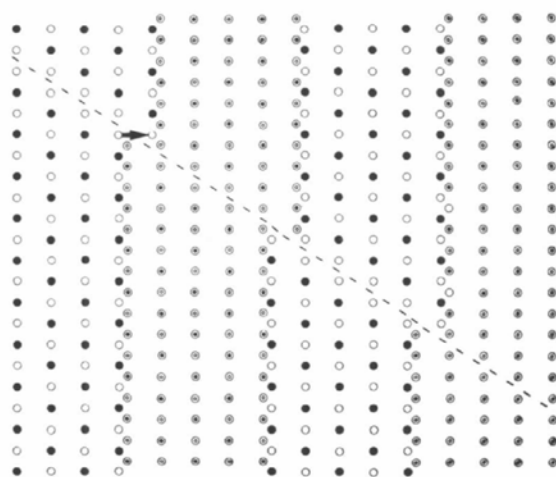

Fig. 16. Model for the antiphase boundary of Fig. 15. The displacement vector is $\frac{1}{2} [001]_{D0_{22}}$ and the boundary plane $(111)_{D0_{22}}$.

References

COENE, W., BENDER, H., LOVEY, F. C., VAN DYCK, D. & AMELINCKX, S. (1985). *Phys. Status Solidi A*, **87**, 483–497.

SCHUBERT, K. (1964). In *Kristallstrukturen Zweikomponentigen Phasen*, p. 92. Berlin: Springer.

TAKEDA, M., VAN TENDELOO, G. & AMELINCKX, S. (1987). *Mater. Res. Bull.* **22**, 1441–1448.

VAN DYCK, D. & COENE, W. (1984). *Ultramicroscopy*, **15**, 29–40.

VAN TENDELOO, G., WOLF R., VAN LANDUYT, J. & AMELINCKX, S. (1978). *Phys. Status Solidi A*, **47**, 539–554.

Analytic Properties of the Contrast Transfer Function in High-Resolution Electron Microscopy

BY PETER REZ

Center for Solid State Science and Department of Physics, Arizona State University, Tempe, Arizona 85287-1504, USA

Abstract

To calculate high-resolution images it is necessary to convolute the wavefunction generated by scattering from the specimen with the microscope objective-lens wavefront aberration function. This is usually done by a multiplication of the transfer function and the specimen exit-surface wavefunction in reciprocal space followed by a numerical integration over all scattering wave vectors. Examination of the analytic behaviour of the wave-front aberration function in the complex plane shows that, for simple scattering functions, it is possible to perform the integral analytically using the method of stationary phase. Analytic results for the imaging of disordered planes of atoms are compared with fast Fourier transform calculations as a function of defocus. The limitations of stationary-phase integration are also discussed.

The calculation of high-resolution images in electron microscopy can be divided into two parts. The amplitude distribution as a function of scattering wave vector is first calculated using some model for the potential in the specimen and an appropriate theory for electron scattering (Spence, 1980). If the scattering is relatively weak the specimen can be considered as either a strong or a weak phase object (Cowley, 1975). Alternatively, a full dynamical diffraction calculation using either Bloch-wave (Bethe, 1928) or multislice methods (Cowley & Moodie, 1957) could be performed to give the wave function at the exit surface of the crystal.

The second part of the calculation considers the effects of the microscope objective lens and its aberrations in forming the image. This could be done by a convolution in real space but it is more convenient to replace this by a multiplication of the exit-surface wavefunction and the wave-front aberration functions in reciprocal space followed by an integration over all relevant scattering wave vectors (Spence, 1980). The wave-front aberration is an additional phase function $\exp[i\chi(\mathbf{u})]$ where

$$\chi(\mathbf{u}) = (\pi/\lambda)[(C_s/2)\lambda^4 u^4 - f\lambda^2 u^2], \qquad (1)$$

where $\mathbf{u}$ is the scattering wave vector, λ is the electron wavelength, f is the defocus and C_s is the lens spherical aberration.

For high-energy electrons, scattering angles are small and the scattering wave vector is assumed to lie in a plane parallel with the specimen surface. It is then more convenient to write the wave-front aberration function in terms of the scattering angle

$$\chi(\theta) = (\pi/\lambda)[(C_s/2)\theta^4 - f\theta^2]. \qquad (2)$$

Crystals scatter in directions given by the Bragg angles θ_g for the various crystal planes. The image amplitude is then given by

$$A(\mathbf{r}) = \sum_{\theta_g} \psi(\theta_g) \exp[i\chi(\theta_g)] \exp(2\pi i r \theta_g/\lambda) \qquad (3)$$

where $\psi(\theta_g)$ are the complex scattering amplitudes for diffraction from the crystal (Spence, 1980). For single-atom scattering (Chiu & Glaeser, 1975) or scattering by amorphous objects or defects the summation should be replaced by an integration.

$$A(\mathbf{r}) = \int \psi(\boldsymbol{\theta}) \exp[i\chi(\boldsymbol{\theta})] \exp(2\pi i \mathbf{r} \cdot \boldsymbol{\theta}/\lambda) \, d^2\boldsymbol{\theta}. \qquad (4)$$

In the simplest case we can assume that the scattering is given by the weak-phase-object approximation

$$\psi(\boldsymbol{\theta}) = if_e(\boldsymbol{\theta}) \qquad (5)$$

where $f_e(\boldsymbol{\theta})$ is the electron scattering factor. The